



**HAL**  
open science

## Carrier gradients and the role of charge selective contacts in lateral heterojunction all back contact perovskite solar cells

Sean Dunfield, Aleksandra Bojar, Stefania Cacovich, Mathieu Frégnaux, Talysa Klein, Rosemary Bramante, Fei Zhang, Davide Regaldo, Vincent Dufoulon, Jean-Baptiste Puel, et al.

### ► To cite this version:

Sean Dunfield, Aleksandra Bojar, Stefania Cacovich, Mathieu Frégnaux, Talysa Klein, et al.. Carrier gradients and the role of charge selective contacts in lateral heterojunction all back contact perovskite solar cells. *Cell Reports Physical Science*, 2021, 2 (8), pp.100520. 10.1016/j.xcrp.2021.100520 . hal-03336761

**HAL Id: hal-03336761**

**<https://hal.science/hal-03336761>**

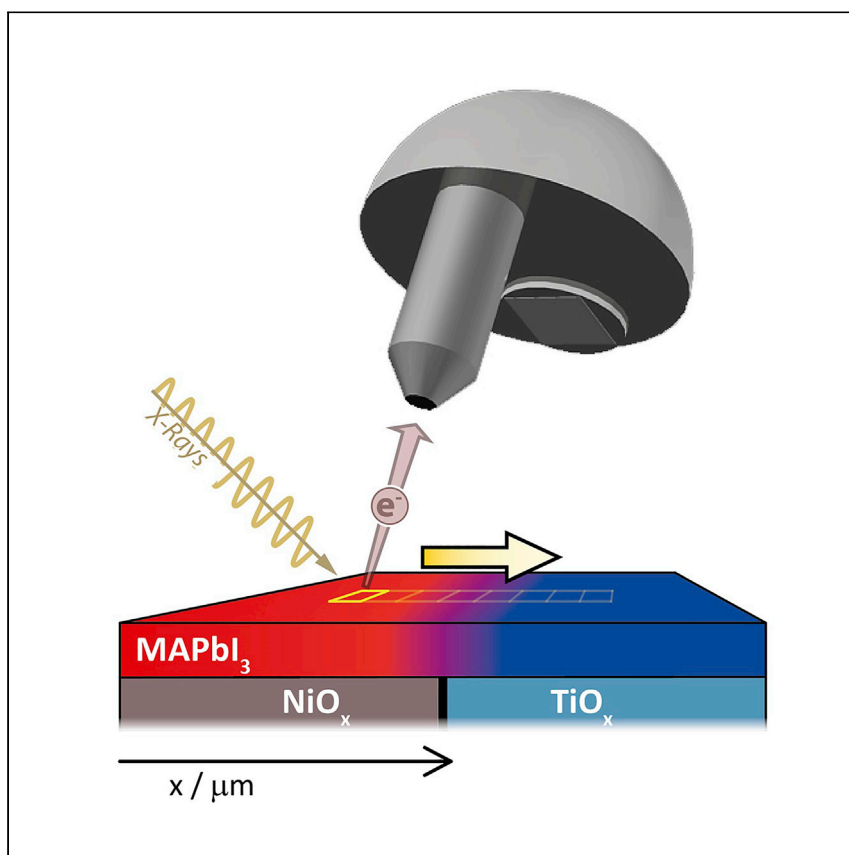
Submitted on 27 Oct 2021

**HAL** is a multi-disciplinary open access archive for the deposit and dissemination of scientific research documents, whether they are published or not. The documents may come from teaching and research institutions in France or abroad, or from public or private research centers.

L'archive ouverte pluridisciplinaire **HAL**, est destinée au dépôt et à la diffusion de documents scientifiques de niveau recherche, publiés ou non, émanant des établissements d'enseignement et de recherche français ou étrangers, des laboratoires publics ou privés.

Article

# Carrier gradients and the role of charge selective contacts in lateral heterojunction all back contact perovskite solar cells



Metal halide perovskites (MHPs) define an emerging field of novel optoelectronics. For MHP-based applications, such as interdigitated back contact solar cells, the right choice of charge selective contacts remains the principal challenge to overcome; however, relatively few design rules exist because of the unusual defect properties of MHPs. Here, Dunfield et al. employ a range of techniques to discern the role of selective contacts.

Sean P. Dunfield, Aleksandra Bojar, Stefania Cacovich, ..., Jean-Paul Kleider, Joseph J. Berry, Philip Schulz

sean.dunfield@nrel.gov (S.P.D.)  
joe.berry@nrel.gov (J.J.B.)  
philip.schulz@cns.fr (P.S.)

### Highlights

Charge selective contacts shift the Fermi level in metal halide perovskites (MHPs)

Effect is readily observable because of low defect and doping concentrations in the MHP

Contact selectivity determines carrier extraction across MHP/contact interfaces

Tailoring charge selective contacts to design MHP-based lateral heterojunction devices

Dunfield et al., Cell Reports Physical Science 2, 100520  
August 18, 2021 © 2021 The Author(s).  
<https://doi.org/10.1016/j.xcrp.2021.100520>



Article

# Carrier gradients and the role of charge selective contacts in lateral heterojunction all back contact perovskite solar cells

Sean P. Dunfield,<sup>1,2,\*</sup> Aleksandra Bojar,<sup>3,4</sup> Stefania Cacovich,<sup>3,6</sup> Mathieu Frégnaux,<sup>3,7</sup> Talysa Klein,<sup>1</sup> Rosemary Bramante,<sup>1</sup> Fei Zhang,<sup>1</sup> Davide Regaldo,<sup>3,4</sup> Vincent Dufoulon,<sup>3,6</sup> Jean-Baptiste Puel,<sup>3,9</sup> Glenn Teeter,<sup>1</sup> Joseph M. Luther,<sup>1</sup> Muriel Bouttemy,<sup>3,7</sup> Dennis Nordlund,<sup>8</sup> Kai Zhu,<sup>1</sup> David T. Moore,<sup>1</sup> Maikel F.A.M. van Hest,<sup>1</sup> Jean-Paul Kleider,<sup>3,4,5</sup> Joseph J. Berry,<sup>1,\*</sup> and Philip Schulz<sup>3,6,10,\*</sup>

## SUMMARY

Realizing photovoltaic devices that achieve the full potential of the metal halide perovskite material will require improved insight regarding the role of selective contacts and how key interfaces operate when mobile defects are present. However, measuring interface properties in typical device stacks where the perovskite layer is thin and sandwiched between two contacts has been a challenge. Here, we fabricate p-i-n and p-n lateral heterojunctions with nickel oxide/titanium oxide all back contacts, permitting us to employ a comprehensive analysis approach, including ultraviolet and X-ray photoemission spectroscopy (UPS/XPS), angle-resolved X-ray absorption spectroscopy (XAS), Kelvin probe force microscopy (KPFM), surface photovoltage (SPV), hyperspectral imaging (HSI), and time-resolved fluorescence lifetime imaging microscopy (TR-FLIM) to discern the role of selective contacts. Specifically, we tune the selectivity of the contacts, changing the gradient in the carrier concentration across the surface of the active layer, which is connected to carrier extraction at the buried interface, and thus the device functionality.

## INTRODUCTION

Optimization of metal halide perovskite (MHP) composition, processing, and device architectures have led to a remarkable rise in perovskite solar cell (PSC) performance. However, further improvements will require additional insights on how its fundamental optoelectronic properties affect device operation. In particular, selective contacts, i.e., contacts that primarily extract one type of charge carrier and block the other, have been proven to be critical to both the efficiency and stability of PSCs.<sup>1</sup> However, to date, the effect of charge selectivity on the optoelectronic properties of the MHP interfaces and bulk remains vague because changes to carrier dynamics are implied but difficult to track, which inhibits us from formulating exact material design strategies for the contact layers.<sup>2</sup> Specifically, in contrast to other more developed technologies, the energy level offsets between the contact layers and the MHP active layer have been suggested to have minimal effect on the device parameters, which are, instead, predominately determined by defects that form at the MHP surfaces/interfaces.<sup>3,4</sup> Assessing the effect of these interfacial interactions on the carrier dynamics of an operating conventionally vertically stacked MHP device has been complicated by the fact that MHP thin film is sandwiched between two

<sup>1</sup>National Renewable Energy Laboratory, 15013 Denver West Pkwy, Golden, CO 80401, USA

<sup>2</sup>Materials Science & Engineering Program, 027 UCB, University of Colorado Boulder, Boulder, CO 80303, USA

<sup>3</sup>IPVF, Institut Photovoltaïque d'Ile-de-France, 18, Boulevard Thomas Gobert, 91120 Palaiseau, France

<sup>4</sup>Université Paris-Saclay, CentraleSupélec, CNRS, Laboratoire de Génie Electrique et Electronique de Paris, 91192 Gif-sur-Yvette, France

<sup>5</sup>Sorbonne Université, CNRS, Laboratoire de Génie Electrique et Electronique de Paris, 75252 Paris, France

<sup>6</sup>CNRS, École Polytechnique, IPVF, UMR 9006, 18, Boulevard Thomas Gobert, 91120 Palaiseau, France

<sup>7</sup>Institut Lavoisier de Versailles, Université de Versailles Saint-Quentin-en-Yvelines, Université Paris-Saclay, CNRS, UMR 8180, 45 avenue des Etats-Unis, 78035 Versailles Cedex, France

<sup>8</sup>SLAC National Accelerator Laboratory, 2575 Sand Hill Rd, Menlo Park, CA 94205, USA

<sup>9</sup>EDF R&D, 91120 Palaiseau, France

<sup>10</sup>Lead contact

\*Correspondence: [sean.dunfield@nrel.gov](mailto:sean.dunfield@nrel.gov) (S.P.D.), [joe.berry@nrel.gov](mailto:joe.berry@nrel.gov) (J.J.B.), [philip.schulz@cnrs.fr](mailto:philip.schulz@cnrs.fr) (P.S.)

<https://doi.org/10.1016/j.xcrp.2021.100520>



contacts. Consequently, the notion of what makes a contact selective is poorly explored in the perovskite community, as are the effects of those defects. However, more generally, the selectivity of an interface is dictated by the ratio of the recombination resistance of minority (blocked) carriers over the ohmic resistance for majority (targeted) carriers.<sup>5–7</sup> Thus, the propensity of an interface to efficiently collect photocurrent, i.e., the low recombination current of minority carriers and the low resistance of majority carriers, depends on the energy level alignment as well as on the nature and density of defects specific to this interface.

As the community pushes the boundaries of MHP-based devices, understanding the role of defects in determining the optoelectronic properties and charge transfer at the device contacts is a primary concern.<sup>4,8</sup> Part of this task is well underway; numerous studies have begun to detail MHP defect structures by generating a range of chemical potentials required for the formation of the materials and the associated formation and transition energies of possible defects (e.g., methylammonium lead iodide [MAPbI<sub>3</sub>],<sup>9</sup> cesium lead bromide [CsPbBr<sub>3</sub>],<sup>10</sup> methylammonium lead bromide [MAPbBr<sub>3</sub>],<sup>11</sup> cesium lead iodide [CsPbI<sub>3</sub>],<sup>12</sup> and formamidinium lead iodide [FAPbI<sub>3</sub>]<sup>13</sup>). Although results vary across compositions, most structurally stable compositions have been suggested to form materials in which detrimental mid-gap defect states have very high formation energies and are, therefore, unlikely to form, whereas shallow band edge defect states are easily created.<sup>9,10,12–14</sup> This has brought forth the notion that MHP's low formation energy, unique band structure, and high ionicity afford it some sort of “capacity for self-healing” or “defect tolerance” by which the formation of mid-gap defects is prevented by the creation of numerous band edge defects that effectively dope the material, rather than providing states deep in the electronic gap that can serve as non-radiative recombination centers and, thereby, limit its quasi-Fermi level splitting ( $\Delta\mu$ ) under illumination.<sup>15–17</sup> Thus, small changes in chemical potential that result from variations in the nucleation or crystallization of the MHP are predicted to have a far greater effect on its carrier concentration than on the maximum  $\Delta\mu$  obtainable.<sup>9,18</sup>

These effects become apparent when MHP thin films are deposited on various substrates, which induce different growth conditions for the MHP because of differences in the surface chemistry and morphology but that also vary in key electronic parameters, such as doping type, carrier concentration, work function (WF), carrier mobility, etc.<sup>18–21</sup> Although it has been well documented that the optoelectronic properties of MHPs can be altered by the choice of selective contacts/substrates,<sup>18–20,22</sup> the energetics at the interface and carrier dynamics across the interfaces and their relationship to associated defect chemistry in a working device have remained elusive because the active layer is buried underneath the top contacts.

Here, we use substrate-based control to manipulate the majority carrier type of the MHP and create functional p-n and p-i-n lateral heterojunctions (LHJs). The built-in potential ( $V_{bi}$ ) in such a device is formed laterally across the junction by the difference in the carrier concentration of the MHP layer on the left and right sides of the junction, which results from the electronic properties and charge selectivity of the contacts underneath. The width of the gap then defines the active area of the LHJ and, conceptually, best corresponds to the device thickness of a conventional, vertically stacked solar cell when considering charge carrier transport, albeit with vastly different dimensions, which will perturb the device physics (e.g., drift versus diffusion).<sup>23–27</sup> Then, we take advantage of the now exposed top MHP interface running perpendicular to the junction to perform a series of surface sensitive characterization techniques and microscopically resolved luminescence probes to correlate the

electronic properties of the patterned substrate with the electronic properties of the MHP surface and carrier extraction properties of the MHP/substrate interface. From these measurements, we can infer the substrate-induced carrier gradient in the MHP layer, the presence or absence of Fermi level ( $E_F$ ) pinning at the top surface, and finally, the mode of device operation in the interdigitated back contact PSCs studied. Moreover, by using nickel oxide with variable oxidation, and therefore selectivity<sup>28,29</sup> for the carrier extraction,<sup>30,31</sup> we are able to show that the selectivity of the contacts induces a gradient in carrier concentration across the active layer that affects device characteristics.

Our approach, which involves characterizing the top surface of MHP LHJ devices with various underlying contacts using ultraviolet and X-ray photoemission spectroscopy (UPS/XPS), angle-resolved X-ray absorption spectroscopy (XAS), Kelvin probe force microscopy (KPFM), surface photovoltage (SPV), hyperspectral imaging (HSI), and time-resolved fluorescence lifetime imaging microscopy (TR-FLIM) to capture the optoelectronic response as a function of the MHP/substrate interface, which opens an avenue for better understanding of the selectivity of contact layer materials and their interaction with the MHP.<sup>23</sup>

## RESULTS

### Characterization of the perovskite above each contact and across the junction

We produced LHJ (Figure 1A) substrates with a spray-coated n-type contact/electron-transport layer, titanium dioxide ( $\text{TiO}_x$ ); and a spray-coated p-type contact/hole transport layer, nickel oxide ( $\text{NiO}_x$ ), separated by a 120  $\mu\text{m}$  channel in which the fluorine-doped tin oxide (FTO) transparent conductive oxide had been removed. Further details on the fabrication procedure are outlined and described in the [Supplemental information](#) (see [Scheme 1](#)).

Next, we deposited  $\text{MAPbI}_3$  and used XPS and UPS to directly access and measure the electronic properties of the  $\text{MAPbI}_3$  surface above each contact. All photoemission spectroscopy (PES) experiments were conducted with low excitation intensities and minimal radiation exposure to minimize beam damage effects, thereby following protocols established in the literature to determine the unperturbed core level positions, WF, and the position of the valence band maximum ( $E_{\text{VBM}}$ ) with respect to the  $E_F$ .<sup>32</sup> Low power XPS I 3d<sub>5/2</sub>/Pb 4f<sub>7/2</sub> core level and UPS valence band maximum (VBM) results, measured far away from the junction ( $\sim 10$  mm), are shown in [Figures 1B–1D](#). At those locations, the distance excited carriers must travel before reaching the junction is substantially further than their diffusion length, suggesting that any influence of the junction remains negligible. Consistent with previous reports, the MHP's core level and VBM position at the surface, which reflects the carrier concentration, is influenced by the substrate.<sup>19–21</sup> Specifically, we observed a shift of the Pb 4f<sub>7/2</sub> and I 3d<sub>5/2</sub> core levels as well as the VBM by  $\sim 550 \pm 50$  meV, with the MHP surface appearing n-type on top of the  $\text{TiO}_x$  contact ( $E_{\text{VBM}} - E_F = 1.31$  eV) and rather intrinsic on the  $\text{NiO}_x$  contact ( $E_{\text{VBM}} - E_F = 0.79$  eV). Consistent with those changes, we see an equal magnitude shift in the WF, indicating constant ionization energy over the probed MHP surface ([Figure S1](#)). Furthermore, there are no indications of a new species in the core level spectral envelopes ([Figure S2](#)), and although overall composition varies from the  $\text{NiO}_x$  side to the  $\text{TiO}_x$  side because of differences in nucleation and crystallization, measurements across a range of stoichiometries (a large excess of methylammonium iodide [MAI], stoichiometric, or a large excess of lead iodide [ $\text{PbI}_2$ ]) show that the change in energetics are not correlated to a change in MHP composition ([Figure S3](#)). Therefore, we attribute this change of

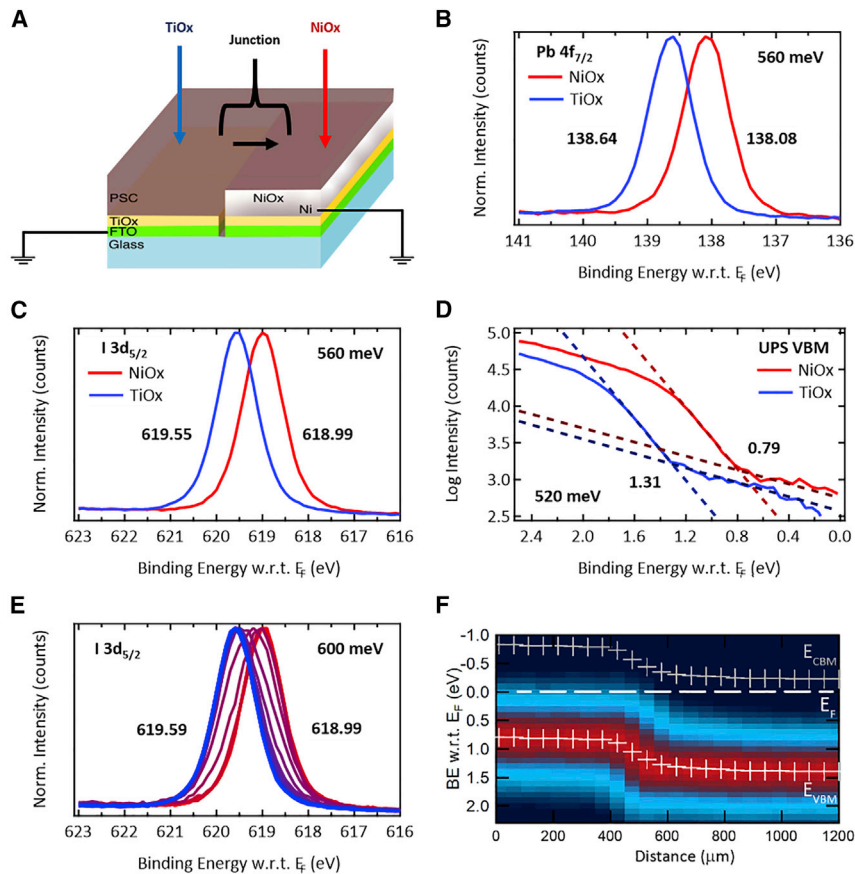


**Figure 1. Photoemission spectroscopy results for a properly oxidized NiO<sub>x</sub>/MAPbI<sub>3</sub>/TiO<sub>x</sub> LHJ**

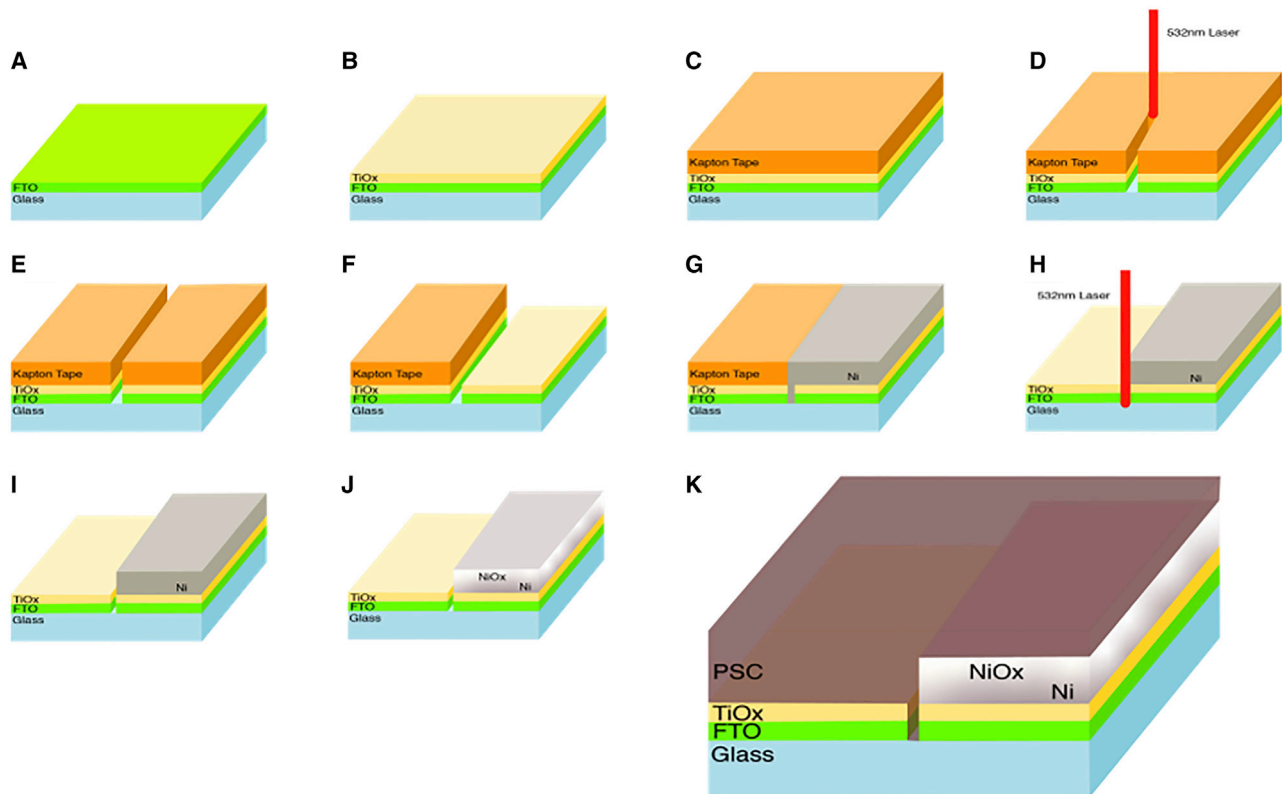
(A) Schematic of a device.

(B–D) Pb 4f<sub>7/2</sub> core levels (B), I 3d<sub>5/2</sub> core levels (C), and UPS VBM spectra (D), taken on the perovskite on top of each contact far away from the junction, show a shift of ~550 meV, which corresponds to a change in the carrier concentration from the n-type to intrinsic.

(E and F) I 3d<sub>5/2</sub> core level measurements (E) and associated false-color plot (F) of the junction as a function of sample position scanned across the channel. White crosses indicate the projection of the positions of the valence band maximum (E<sub>VBM</sub>) and conduction band minimum (E<sub>CBM</sub>) from the core level peak positions.

surface energetics to a change in carrier concentration induced by the contacts beneath. We note that this does not rule out a compositional gradient across the junction, but given the analysis of multiple compositions, we can exclude compositional variations as the sole explanation for the source of this behavior.

Next, to determine how this carrier concentration evolves across the 120 μm junction between the two contacts, we conducted low power I 3d<sub>5/2</sub> measurements from the NiO<sub>x</sub> side to the TiO<sub>x</sub> side of the junction. Results, displayed in Figures 1E and 1F show a gradual shift in the core level across the surface of the junction, starting and ending near the values measured far away from the junction with only minimal fluctuations because of beam exposure and sample non-uniformity. This variation in energetics in the MHP layer, and thus carrier concentration from side to side, is then equal to the magnitude of the band bending or the achieved V<sub>bi</sub> across the junction.<sup>5</sup> In our scheme here, we track the trend of this band bending across the LHJ MHP surface. Although our results are likely convoluted by a large number of



### Scheme 1. Lateral heterojunction fabrication overview

(A–D) The procedure starts with glass/FTO substrates (A), a  $\text{TiO}_x$  layer is deposited by spray pyrolysis (B), the entire surface is covered in Kapton tape (C), and a strip of Kapton tape/ $\text{TiO}_x$ /FTO is removed down the center of the substrate using a 532 nm laser (D). (E–H) Post-scribe, the sample should look as shown in (E). Then, we remove Kapton tape on one half of the substrate (F), evaporate the nickel (G), and remove the Kapton tape and re-scribe down the center of the substrate to recreate the gap (H). (I) This results in substrates look like this. (J and K) From there, we oxidize the surface of the nickel layer into a  $\text{NiO}_x$  layer (J) and then, deposit the perovskite, resulting in finished LHJ devices (K).

reduced lead centers on the surface of  $\text{MAPbI}_3$ , which act as donor defects and cause the surface, as measured by PES, to appear to be more n-type than the rather intrinsic bulk<sup>33–38</sup>,  $E_F$  at the MHP surface is not completely pinned to the conduction band on either side of the junction. As a result, although the exact  $E_F$  position in the  $\text{MAPbI}_3$  layer at the buried  $\text{MAPbI}_3$ /oxide interface remains unknown in this assessment, the lack of  $E_F$  pinning allows us to follow the gradient in the carrier profile across the bulk of the MHP film set by the contacts. This leads to a remarkable finding: although the effect of the substrate-controlled  $E_F$  positions in MHPs has been consistently shown at the surface of MHP thin films (several 100 nm thick),<sup>19</sup> the gradual shift of  $E_F$  across the LHJ surface observed here suggests that the influence of the substrate is still conveyed over the range of several tens of micrometers. The observation of this behavior can be best described if a low free carrier and defect density in the MHP bulk is assumed, which gives rise to the accordingly large depletion width. This is in line with previous reports on very low defect densities in MHPs in general and in  $\text{MAPbI}_3$  in particular.<sup>39</sup>

To ensure that the observed shift in carrier concentration originates from the buried interfaces and a bulk redistribution of carriers, as has been previously assumed, rather than a dipole on the surface, we conducted angle-resolved XAS measurements.<sup>40,41</sup> In those measurements, we used the site selectivity of a core excitation,

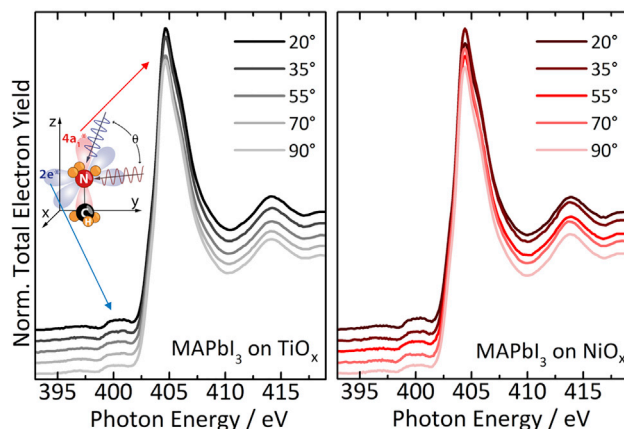


**Figure 2. Angle-resolved XAS results for MAPbI<sub>3</sub> on TiO<sub>x</sub> and NiO<sub>x</sub>**

Results show a lack of angular dichroism, ruling out the possibility that the observed changes in surface energetics originate from a surface dipole because of an orientation of the MA cation.

the highly linearly polarized synchrotron radiation, and the nature of the dipole transition to provide state-specific information on the orientation of functional groups that have well-defined molecular orbitals.<sup>42,43</sup> For MA, the ammonium group has an asymmetry in the molecular orbital that displays an angular dependence in the N 1s XAS spectrum as a function of the angle of incoming light relative to the MA molecular orientation. This can be explored to evaluate whether there is a dipole oriented preferentially to the probed surface orientation—on average—and, thus, discern whether a dipole is formed by the oriented molecular species on the surfaces. The variation or lack thereof in these features as the angle of X-ray incidence is changed then indicates whether a preferential orientation of the individual molecular building blocks, with respect to the sample orientation, is present within the sample volume probed. Results, shown in Figure 2, taken from the total electron yield spectra are representative for the MHP surface region and lack angular dichroism for the nitrogen-related absorption features of the MA, notably the 4a<sub>1</sub>\* transition linked to the 2p<sub>z</sub> orbital and the 2e\* transition linked to the 2p<sub>x</sub> and 2p<sub>y</sub> orbitals,<sup>44</sup> on both NiO<sub>x</sub> and TiO<sub>x</sub>. This indicates that the shift of E<sub>F</sub> is not linked to a near surface (approximately the top 10 nm) MA-dipole orientation. Therefore, the previously reported changes in E<sub>VBM</sub>, WF, and binding energies likely correspond to a shift of E<sub>F</sub> in the gap because of a carrier gradient, which, in turn, affects the photovoltaic activity of the LHJ structure from which a significant contribution of drift current is expected.

#### Device functionality and connection to the built-in potential

To confirm this hypothesis, we fabricated a series of MAPbI<sub>3</sub> LHJ devices using various gap widths from 0.05 mm (just over the size of the laser beam used to make the gap) to 5 mm. Current density-voltage (J-V) results are shown in Figure 3. Increasing the width of the gap results in large reductions to current density and the fill factor but leaves the open-circuit voltage (V<sub>oc</sub>) of the device relatively unaffected, with a minimum value of ~400 mV and a maximum value of ~500 mV. Moreover, reducing the gap width to zero, such that the device now resembles a p-n junction, rather than a p-i-n junction, produces devices with unmeasurable current because of the shunts between the contacts but a similar gradient in carriers, as measured by PES (Figure S4). This suggests that, although the large gap/junction width inhibits the charge transport, the extraction of carriers from the device occurs at a voltage



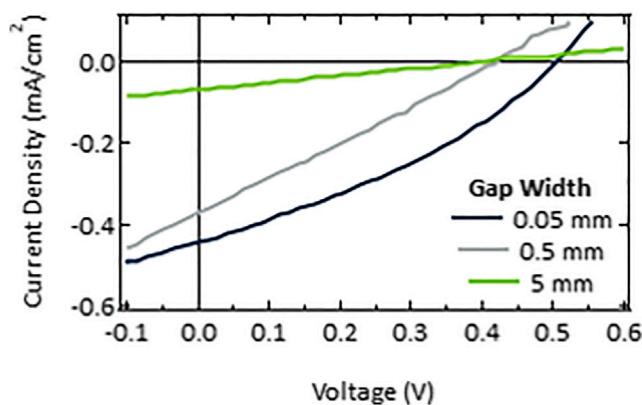


**Figure 3. J-V results for a well-oxidized NiO<sub>x</sub>/MAPbI<sub>3</sub>/TiO<sub>x</sub> LHJ as a function of gap width**  
Results show a relatively constant open-circuit voltage across all gap widths.

difference that can be correlated to the gradient in the carrier concentration between the regions of the MHP film grown on TiO<sub>x</sub> and NiO<sub>x</sub>, as inferred from the PES measurements conducted at the surface. However, we note that although the  $V_{bi}$  measured at the surface and the  $V_{oc}$  of the device appear to be nearly equivalent here, this is not expected to always be the case; deviations between the two are anticipated if the MHP has a varied surface band bending across the junction such that the surface gradient is not representative of the bulk gradient or if the gap between the electrodes is small enough to collect a diffusion-based current. Moreover, losses to the obtainable photovoltage can be expected because of interfacial recombination at the contact. Thus, despite being nearly equal here, the  $V_{bi}$  and  $V_{oc}$  would be expected to vary in devices with junction sizes approximately equal to the MHP diffusion length due to the diffusion-based contributions to the current. Nevertheless, a strong built-in potential is a driving force for the current and can therefore be correlated to better device parameters in most systems, even those with significant diffusion-based current contributions. To confirm that this gradient is facilitated by the selectivity/ $V_{bi}$  between the MHP on the two contacts and not an alternative phenomenon, e.g., polarization,<sup>45</sup> symmetric TiO<sub>x</sub>/TiO<sub>x</sub> and NiO<sub>x</sub>/NiO<sub>x</sub> MHP LHJ control devices were fabricated and tested. J-V results, shown in Figure S5, are in line with expectations, showing little to no photoactivity or rectification, likely because of the lack of selectivity in the contacts/ $V_{bi}$  between the MHP on the two contacts.

### Changing the NiO<sub>x</sub> layer to alter selectivity

Having shown that the LHJ between the TiO<sub>x</sub> and NiO<sub>x</sub> is afforded by the different contacts, we shifted focus to characterizing how the junction in the otherwise identically processed MHP layer changes as the selectivity and morphology of the NiO<sub>x</sub> contact is altered while the TiO<sub>x</sub> is kept the same. We, hence, created another set of samples by e-beam evaporating nickel then oxidizing it in air. This allowed us to create thinner, smoother, and more compact films, whose level of surface oxidation could be altered by changing annealing conditions. Thus, we produced two LHJ samples with 150 nm thick e-beam-deposited nickel: one where the nickel was heavily oxidized using a robust annealing procedure similar to the spray-coated NiO<sub>x</sub>; and one where it was lightly oxidized at a lower temperature for a shorter duration so that the conversion from nickel (metallic) to NiO<sub>x</sub> (p-type) was incomplete. Analysis of representative substrates is included in Figures S6 and S7. From that sample set it is clear that (1) increasing the annealing temperature increases the amount of NiO formed and decreases the amount of

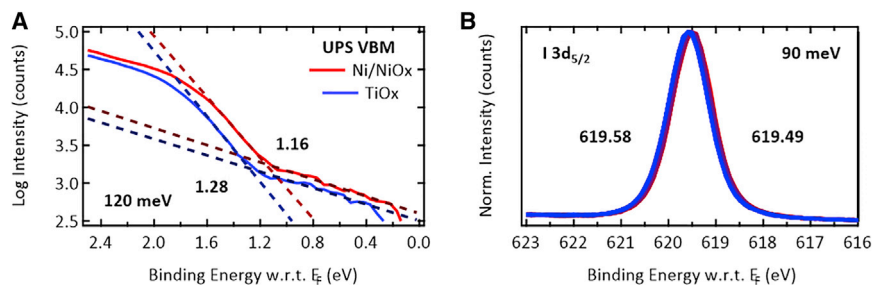


**Figure 4. Photoemission spectroscopy results for a NiO<sub>x</sub>/MAPbI<sub>3</sub>/TiO<sub>x</sub> LHJ using a less-oxidized nickel oxide (Ni/NiO<sub>x</sub>) contact**

(A) UPS VBM spectra taken on the perovskite on top of each contact far away from the junction indicate a substantially smaller shift of  $\sim 120$  meV compared to  $\sim 520$  meV in Figure 1D.

(B) I 3d<sub>5/2</sub> core level measurement across the junction show that this potential gradually drops across the junction.

metallic nickel and Ni(OH)<sub>2</sub>/NiOOH redox states, and (2) qualitatively similar films can be created from evaporation and solution deposition. It is also clear that the amount of native oxide on the surface of the films, which can be altered by small changes in handling, processing, or environmental conditions, will alter the overall oxidation state of the Ni/NiO<sub>x</sub> and, therefore, its associated energetics.<sup>46–48</sup> Moreover, as shown in Figure S8, the MAI species present in our MHP composition readily reacts with the NiO<sub>x</sub> surface to increase the amount of Ni(OH)<sub>2</sub>/NiOOH groups present with respect to (w.r.t.) the NiO.<sup>30</sup> Therefore, these results qualitatively show that increasing the annealing temperature increases the amount of NiO in the films w.r.t the metallic nickel, moving the VBM from a degenerate position in the case of the native oxide to  $\sim 550$  meV for the 300°C annealed sample.

With a qualitative understanding of how the substrates should change with the lesser oxidation, we deposited MAPbI<sub>3</sub> on the adapted substrates and conducted low power I 3d<sub>5/2</sub> core level measurements to compare the difference in  $E_F$  from side to side to the results above. Results from measurements taken far away from the junction ( $\sim 10$  mm), shown in Figure S9, indicate a nearly identical shift in the  $E_F$  of the MHP on TiO<sub>x</sub> to NiO<sub>x</sub> for the sample with the robust anneal as the sample with spray-coated NiO<sub>x</sub>. In contrast, results for the less-oxidized nickel sample (hereafter referred to as Ni/NiO<sub>x</sub>) show a far smaller splitting between the two sides because of a shift in the core level of the MHP on the Ni/NiO<sub>x</sub> side (plotted against the more-oxidized case in Figure S9 for clarity). To confirm that this different magnitude potential exhibits a similar drop across the junction as the more-oxidized spray-coated sample, we conducted UPS VBM measurements far away from the junction (Figure 4A) as well as XPS I 3d<sub>5/2</sub> core level measurements across the junction (Figure 4B) on the less-oxidized sample. As above, measurements indicate that the selectivity of the contact induces a carrier concentration in the MHP directly above the contacts and a gradient between them. However, this time we see an  $\sim 450$  meV smaller shift across the junction because of the less-thorough oxidation of the Ni/NiO<sub>x</sub> contact, which induces a change in the chemical potential.

To better understand the electrostatic potential variations at equilibrium in the two different LHJ samples, we modeled the system with the help of the 2D drift-diffusion software Silvaco Atlas. Specifically, we fixed the MHP layer ionization energy (the location of the valence band w.r.t. the vacuum level) and electron affinity (the location of the conduction band w.r.t. the vacuum level), as determined from XPS/UPS

(assuming a band gap of 1.55 eV); then, we adjusted other parameters (Table S1) to replicate the potential drop observed across the junction for the two different devices. As can be seen, we used very similar values to the electron affinity, WF, and ionization potential determined from XPS/UPS (assuming a band gap of 3.2 eV) for the TiO<sub>x</sub> side. In contrast, for the Ni/NiO<sub>x</sub> side, we used literature-reported values consistent with a more- and less-oxidized nickel sample.<sup>46–48</sup> We did this because the variability of Ni/NiO<sub>x</sub> in air prohibited us from making accurate measurements with KPFM, whereas its sensitivity to UV light (Figure S10 versus Figure S11) prohibited us from making accurate measurements with our UPS setup. In addition, the surface chemistry of NiO<sub>x</sub> is expected to change upon MHP deposition. Results for the more- and less-oxidized cases, shown in Figures S12 and S13, are consistent with the XPS results across the junction for both cases. Moreover, results shown in Figure S14, indicate that increasing the acceptor carrier concentration of the MHP layer past  $\sim 10^{13}/\text{cm}^3$  causes the profile across the junction to deviate from what was observed in XPS/UPS for the more-oxidized case (Figure 1). This provides further evidence that a gradient in equilibrium electrostatic potential, and thus a carrier concentration similar to the observed ones, can prevail over tens of microns if the MHP material is almost undoped.

### Understanding carrier dynamics

Having tied the  $V_{\text{bi}}$  measured by PES to the selectivity of the contacts, we further validated that our measurements reflect the equilibrium dark carrier concentration gradient and are not compounded by photovoltage induced by the excitation source.<sup>49,50</sup> To do so, we conducted KPFM and SPV measurements on the less-oxidized Ni/NiO<sub>x</sub> sample from the PES experiments. In these techniques, a conductive atomic force microscope (AFM) tip is used as a Kelvin probe to track the contact potential difference (CPD) between the surface potential of the tip and the surface potential of the sample, creating a high-resolution topography map with a corresponding CPD distribution. However, unlike PES-based techniques, these measurements provide a probe of energetics without using optical excitation, especially if the system is tracked with a laser below the band gap of the semiconductor.<sup>51</sup> Therefore, in our study, in which we used a 0.95 eV infrared (IR) laser, the CPD values measured in the dark should represent the dark state of the material's equilibrium. Performing subsequent measurements over the same area under illumination then allows us to monitor light-induced changes in the surface potential of the sample.

The SPV is then simply the difference between the CPD values measured under illumination ( $\text{CPD}_{\text{light}}$ ) and in the dark ( $\text{CPD}_{\text{dark}}$ ). In single-layered structures (i.e., MHP on a grounded conductor), the SPV can be directly related to the separation of photogenerated charge carriers—with its magnitude proportional to the amount of the separated charge and its sign indicative of the type of carrier measured at the surface, whether electronic or ionic.<sup>52</sup> However, a mobile charge at the surface can be perturbed by changes in many factors in the bulk, surfaces, and interfaces of the MHP<sup>53</sup> as well as in carrier dynamics within the sample (e.g., charge carrier accumulation, recombination, extraction, and/or trapping).<sup>49,54–57</sup> Therefore, in multilayered structures, SPV can also be affected by carrier dynamics (in the oxide or MHP layer) and interfacial chemical reactions occurring between the two semiconductors. Specifically, a conductor/semiconductor/MHP structure grounded by the conductor will witness a decrease in CPD (causing a negative SPV) if holes are extracted from the MHP or if a negative charge accumulates at the surface. Thus, in our system, which has selective contacts and donor defects at the surface, the TiO<sub>x</sub> side is anticipated to have counteracting SPV effects, with a positive contribution from the extraction of electrons by TiO<sub>x</sub> (Figure S15A) and a negative contribution from

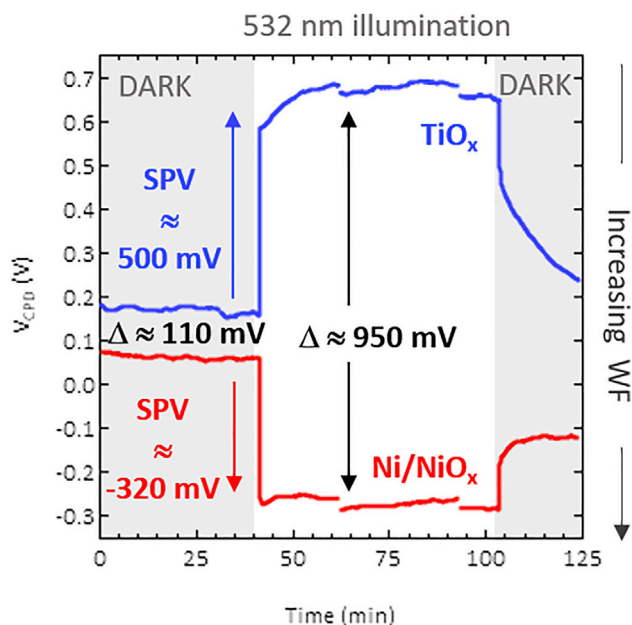


**Figure 5. KPFM and SPV results for a  $\text{NiO}_x/\text{MAPbI}_3/\text{TiO}_x$  LHJ using a less-oxidized nickel oxide ( $\text{Ni}/\text{NiO}_x$ ) contact**

Average CPD evolution as a function of time and illumination conditions for the perovskite on the  $\text{TiO}_x$  and  $\text{Ni}/\text{NiO}_x$  sides. Measurements taken in the dark show a 110 mV CPD difference between the two sides in the dark, in agreement with XPS measurements across the junction. Upon illumination, a positive SPV of 500 mV is observed for the perovskite on  $\text{TiO}_x$ , which can be attributed to the opposing effects of electron accumulation at the front interface and electron extraction at the back interface. In contrast, the  $\text{NiO}_x$  sees a 320 mV decrease in SPV because of the combined effects of electron accumulation at the front and the hole extraction at the back. This implies the perovskite or interface is worse on the  $\text{Ni}/\text{NiO}_x$  side than on the  $\text{TiO}_x$  side.

photogenerated electrons filling surface donor states (Figure S15B). In contrast, the  $\text{Ni}/\text{NiO}_x$  side will have aligning negative contributions to the SPV from the extraction of holes and the filling of surface donor states with electrons. Therefore, although KPFM/SPV measurements cannot quantitatively discern the relative contributions from the effects, they can be used to infer the mobile charge concentrations in the near-surface region and to set limits on their response to the photoexcitation of the sample. Conducting these measurements far away from the junction, for which the movement of the mobile charge will not be perturbed by the other contact, then allows us to probe the combined effects of photocarrier generation, extraction, and recombination on the net carrier concentrations of the MHP material on each selective contact.<sup>53</sup>

KPFM results taken in the dark on the plain substrates are shown in Figure S16. They are consistent with the  $\text{Ni}/\text{NiO}_x$  being less oxidized, showing only  $\sim 350$  meV difference between the two contacts as opposed to the commonly reported difference of 1 eV for well-oxidized  $\text{NiO}_x$  and  $\text{TiO}_x$  surfaces.<sup>21,58</sup> KPFM results for the MHP on top of both the  $\text{Ni}/\text{NiO}_x$  and  $\text{TiO}_x$  halves in both dark and light conditions are shown in Figure 5. The average CPD values are extracted from the  $3 \times 3 \mu\text{m}^2$  CPD maps, which are presented in the Supplemental information (Figure S17), together with representative topography of the substrates and the MHP layer (Figure S18). The difference in CPD between the two sides is  $\sim 110$  mV (compared with the  $\sim 120$  meV and  $\sim 90$  meV measured in UPS and XPS, respectively), which confirms that the carrier concentration gradient is present under equilibrium dark conditions.

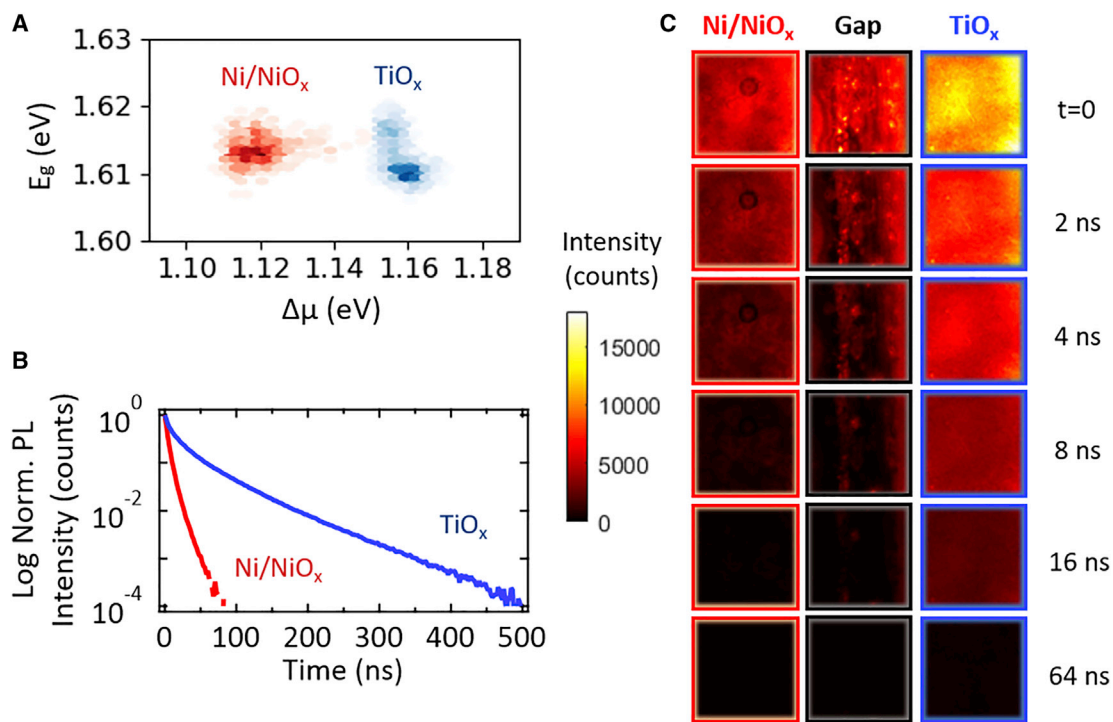


**Figure 6. Multidimensional photoluminescence imaging results**

(A) Hyperspectral imaging fitting results for every pixel for the MAPbI<sub>3</sub> film on TiO<sub>x</sub> and Ni/NiO<sub>x</sub>, where darker colors indicate more counts.

(B) Photoluminescence decays for MAPbI<sub>3</sub> on top of Ni/NiO<sub>x</sub> and TiO<sub>x</sub>.

(C) The 133  $\mu\text{m} \times 133 \mu\text{m}$  TR-FLIM images display the evolution of photoluminescence intensity on the TiO<sub>x</sub> half, in the gap, and on the Ni/NiO<sub>x</sub> half. Results indicate a worse rate of extraction to recombination on the Ni/NiO<sub>x</sub> half.

Upon illumination, the redistribution of photogenerated charges causes the CPD to change. For the MHP on TiO<sub>x</sub>, we measure an increase in CPD on the order of  $\sim 500$  mV because of the opposing effects of electron extraction at the back interface and accumulation at the front interface (Figures S17 and S18). For the Ni/NiO<sub>x</sub> half, we measure a decrease in the CPD on the order of  $\sim 320$  mV from the combined effects of hole extraction and electron accumulation. The relative SPV contributions align in the Ni/NiO<sub>x</sub> half and counteract in the TiO<sub>x</sub> half, which implies that the MHP film on Ni/NiO<sub>x</sub> has worse extraction properties and/or higher rates of recombination than the film on the TiO<sub>x</sub>. When the light is turned off, SPV relaxation takes place. The fast component corresponds to electronic relaxation, whereas the slower ones may be attributed to ion migration.<sup>49,59</sup> As shown in Figure 5, the SPV slowly relaxes to its original value for the TiO<sub>x</sub> side but not for the Ni/NiO<sub>x</sub> side, indicating a modification in the static potential of the MHP surface.<sup>49</sup> We attribute that to chemical reactions at both sides of the MHP, namely, those between nickel and the MHP<sup>20,30</sup> and those between the iodide vacancies at the MHP surface and oxygen.<sup>2,60,61</sup> These reactions likely become visible after prolonged (i.e., days) exposure (Figure S19).

To further investigate optoelectronic and transport properties of the MAPbI<sub>3</sub> layer in the LHJ, we employed multidimensional photoluminescence imaging, i.e., HSI<sup>62</sup> and TR-FLIM.<sup>63</sup> The HSI acquires spectrally resolved, calibrated spectrum images, giving access to the photoluminescence intensity ( $I_{PL}$ ) in absolute units. We first performed steady-state measurements on MAPbI<sub>3</sub>, deposited on different substrates, and fitted the photoluminescence (PL) spectra by using the approach proposed by

Katahara and Hillhouse,<sup>64,65</sup> based on the Planck generalized law, combined with sub-band gap-absorption properties:

$$I_{PL}(E) = \frac{2\pi}{h^3 c^2} \frac{E^2 a(E)}{\exp\left(\frac{E-\Delta\mu}{kT}\right) - 1}$$

where  $h$  is the Planck constant,  $c$  is the speed of light,  $E$  is the photon energy,  $a(E)$  is the absorptivity of the sample taking into account the sub-band-gap absorption,  $\Delta\mu$  is the quasi-Fermi level splitting, and  $kT$  is the thermal energy of the charge carriers. Results from fitting measurements conducted at 10 suns (Figure S20A) show that the Ni/NiO<sub>x</sub> side has an identical band gap (1.61 eV) but a slightly lower  $\Delta\mu$  (1.12 eV) compared to that of the TiO<sub>x</sub> side (1.16 eV). This indicates that the MHP material quality does not limit the  $V_{oc}$  obtained in our device configuration. Moreover, assuming the bulk properties are identical in the two cases, the 40 meV difference can be ascribed to higher rates of recombination processes occurring at the (Ni/NiO<sub>x</sub>)/MAPbI<sub>3</sub> interface than occurred at the TiO<sub>x</sub>/MAPbI<sub>3</sub> interface, in line with the KPFM/SPV results.<sup>66</sup> In addition to lower rates of recombination, the TiO<sub>x</sub> side also exhibits more homogeneous optoelectronic properties, as highlighted in Figure 6A, in which  $\Delta\mu$  is plotted as a function of the energy gap for every measured location. The transport properties were then probed by acquiring TR-FLIM images, reported in Figure 6C. The decay values (Figure 6B) are significantly faster in the case of the Ni/NiO<sub>x</sub> contact, which is consistent with the presence of more non-radiative recombination processes at the interface between Ni/NiO<sub>x</sub> and MHP than at the TiO<sub>x</sub>/MHP interface, confirming the HSI and KPFM/SPV results. Moreover, the lifetime measured near the junction on each of the respective contacts appears to track with that measured far away from the junction. This is also in line with the steady-state measurements showing a higher value of  $\Delta\mu$ , indicating that the carrier concentration gradient at the surface, as measured by XPS, correlates well with other optoelectronic data and associated material properties (e.g.,  $\Delta\mu$ ) of the sample, which are largely dictated by the bottom contact.

Although the in-depth analysis of the role of selective contacts was only conducted for MAPbI<sub>3</sub>, similar carrier concentration gradients and/or the device  $V_{oc}$  can be obtained for a variety of MHP films with alternate compositions (Figures S21 and 22) and solvent systems (Figure S23). Consequently, we expect the behavior here to be typical of the current class of polycrystalline MHP materials. Specifically, we expect these compounds to be intrinsic, with photovoltaic activity partially originating from the gradient in carrier concentration caused by the selective contacts. We note that although the exact carrier concentrations of the “intrinsic” MHP can be altered by slight deviations to the solution stoichiometry and processing conditions, the gradual drop in potential we observed across the junction necessitates that all samples studied have a quasi-intrinsic MHP with low carrier and defect concentrations.

## DISCUSSION

In this work, we have extensively probed the origins of photovoltaic activity in MHP LHJ devices as well as the root cause of substrate-induced carrier concentrations in the MHP layer. Specifically, by combining XPS, UPS, XAS, KPFM, SPV, HSI, and TR-FLIM measurements, we have shown that the selectivity of the n- and p-type substrates changes the relative carrier concentrations and dynamics in the otherwise intrinsic MHP layer above, suggesting a large depletion width and low defect concentrations. This effect can be taken advantage of to produce LHJs, for which the tailored selectivity of the contacts sets the carrier concentrations of the MHP above the contacts, and thus, in turn, the drop in  $V_{bi}$  between the two contacts.

Here, our analysis of the LHJ architecture renders visible the link between the carrier gradient in the MHP at each end of the junction and photovoltaic performance. Although this gradient in the MHP layer is determined by interactions with the contact layer underneath and appears to correlate with the energetics of the contacts, the discrepancy between potential drop between the contacts pre-MHP deposition and the  $V_{bi}$  across the active layer (e.g., 350 meV from the  $TiO_x$  to the poorly oxidized Ni/NiO<sub>x</sub> pre-MHP deposition versus ~120 meV across the MHP on top) necessitates a more complex picture w.r.t. charge transfer at the buried interface. When combined with previous results that show a lack of correlation between the WF or ionization energy of a range of contacts with varied functional groups and device performance,<sup>3</sup> this research suggests that the energetics of the contacts may not be the dominant driver for selectivity. Therefore, additional work must be performed to determine what makes a MHP contact selective and how that is related to energetics, interface recombination, and the chemical species present at the interface; all of which can be tailored by adapting new contact layer materials, changing the level of oxidation of the contact, or introducing interfacial layers for passivation.

## EXPERIMENTAL PROCEDURES

### Resource availability

#### Lead contact

Further information and requests for resources and materials should be directed to, and will be fulfilled by, the lead contact, Philip Schulz ([Philip.Schulz@cns.fr](mailto:Philip.Schulz@cns.fr)).

#### Materials availability

This study did not generate new unique materials.

#### Data and code availability

The published article includes all data analyzed and necessary to draw the conclusions of this study in the figures and tables of the main text and in the [supplemental information](#). Further information and requests for further data should be directed to the lead contact.

### Materials

Unpatterned TEC 15 (~15 Ω/square) fluorine doped tin-oxide-coated glass substrates were purchased from Hartford Glass. Lead (II) bromide ( $PbBr_2$ , 99.98% metals basis), lead (II) iodide ( $PbI_2$ , 99.9985% metals basis), and nickel formate were purchased from Alfa Aesar. Methylammonium bromide (MABr), methylammonium chloride (MACl), and formamidinium iodide (FAI) were purchased from Dyesol. Cesium iodide (CsI) (99.9% trace metals basis) and a titanium diisopropoxide bis(acetylacetonate) solution (75% in 2-propanol) were purchased from Sigma-Aldrich. All solvents, including acetylacetone, ethylene glycol, ethylene diamine, dimethyl sulfoxide, dimethylformamide, and 1-methyl-2-pyrrolidone, were purchased from Sigma-Aldrich.

### LHJ fabrication

Lateral heterojunction substrates were cut to size, cleaned, and then fabricated as outlined in [Scheme 1](#). Briefly, fluorine-doped tin oxide (FTO) substrates were uniformly coated with 40–60 nm of compact blocking  $TiO_x$ , covered with Kapton tape, and then laser scribed down the center to isolate the two sides. One half of the Kapton tape was then removed, and the freshly exposed side of the substrate was covered with ~1 μm of spray or 150 nm of evaporated nickel, followed by a second scribe to set the width of the junction/gap. Then, the Kapton tape underneath the nickel on the other side was removed to delaminate the nickel above it, leaving a nickel/scribe/ $TiO_x$  junction. Finally, before deposition of the perovskite layer,

samples were UV/ozone (UVO) treated and then annealed in air to oxidize the nickel. Between steps, substrates were kept in a N<sub>2</sub> flowbox filled with desiccant.

### Substrate preparation/cleaning

FTO substrates were ordered in 6 × 6-inch sheets and cut to 1 × 1-inch pieces using a diamond scribe. To ensure uniform coating, the outside perimeter of 1 × 1-inch pieces was not used. The remaining pieces were first manually scrubbed with an ultrasonic toothbrush and 5% solution of Liquinox in deionized (DI) water to remove any debris. Then, substrates were loaded into a holder and sonicated in a Liquinox:DI (5%), DI, acetone, isopropyl alcohol (IPA), and then, methanol for 20 min each. Finally, before deposition of the TiO<sub>x</sub> layer, substrates were UVO-treated for 15 min and then placed on the hotplate for TiO<sub>x</sub> deposition.

### TiO<sub>x</sub> deposition

A TiO<sub>x</sub> precursor solution was obtained by mixing 0.6 mL of a titanium diisopropoxide bis(acetylacetonate) solution (75% in 2-propanol) with 0.4 mL of acetylacetonate and stirring. Once fully dissolved, the precursor solution was loaded into the syringe pump in preparation for coating. Immediately after UVO-treatment, FTO-coated samples (Scheme 1, A) were loaded onto a hotplate and ramped for 450°C. After reaching thermal equilibrium, a compact ~40 nm layer of TiO<sub>x</sub> was deposited by spray pyrolysis in air. To properly convert the TiO<sub>x</sub> to the anatase phase, substrates were left to anneal for 30 min.

### NiO<sub>x</sub> spray deposition

A NiO<sub>x</sub> precursor solution was obtained using a multistep process. First, 1 M (148.77 g) of nickel formate was dissolved in 5 M (278.6 mL) of ethylene glycol to produce a viscous, green-colored solution. Then, 2 M (133.306 mL) of ethylene diamine was added dropwise to the solution, and the solution was quickly agitated, causing it to undergo a highly exothermic reaction and turn purple. Before deposition, the solution was filtered using a 0.2 μm polytetrafluoroethylene (PTFE) filter and then loaded into a syringe in a glove box for deposition. After laser scribing and a 10 min UVO treatment, the substrates with FTO/TiO<sub>x</sub> on one half and FTO/TiO<sub>x</sub>/Kapton tape on the other (Scheme 1, G) were loaded into a glove box and placed on a hotplate, which was ramped to 275°C. After reaching thermal equilibrium, a mesoporous layer of ~1 μm of nickel was deposited via ultrasonic spray deposition of the precursor solution onto the substrates. To ensure even coating, substrates were coated 15 times with a 5 min annealing time between the passes to let the solvent dry. After deposition, the substrates were annealed in the glove box at 275°C for 2 h to form the mesoporous nickel layer. Before deposition of the perovskite layer, substrates were UVO-treated for 10 min and then annealed for 3.5 h in air at 300°C to properly oxidize the nickel.

### NiO<sub>x</sub> evaporation

After the laser scribe and a 10 min UVO treatment, substrates with FTO/TiO<sub>x</sub> on one half and FTO/TiO<sub>x</sub>/Kapton tape on the other (Scheme 1, G) were loaded into a thermal evaporator, where ~150 nm of nickel was deposited at a rate of 0.1 Å/s for the first 10 nm and then 1 Å/s for the rest. Before deposition of the perovskite layer, substrates were UVO-treated for 10 min and then annealed for 30 min in air at 275°C or 2 h in an oven at 300°C to properly oxidize the nickel.

### Laser scribing

Laser scribing was done on a SpectraPhysics Talon-6W 355 nm q-switched Yd:NFL laser with a pulse duration of less than 25 ns at 100 kHz using a custom-built setup.



This setup forces the 1 mm Gaussian beam produced by the laser through two cross-polarizer attenuators, where it reflects off a coated mirror, passes through a fused silica window into a nitrogen-filled glove box, and is focused by a 100 mm focal length lens onto the samples. All laser scribes were completed using  $\text{power}_{\text{ave}} = 0.5 \text{ W} \pm 0.01 \text{ W}$ ,  $\text{rate}_{\text{rep}} = 20 \text{ kHz}$ , and  $\text{distance}_{\text{lens}} = 110 \text{ mm} \pm 1 \text{ mm}$  with different rates. For the initial scribe, we used a  $\text{rate}_{\text{feed}} = 5 \text{ mm/s}$ ,  $\text{distance}_{\text{raster}} = 0 \text{ mm}$ , and  $\text{distance}_{\text{gap}} = 0.05 \pm 0.01 \text{ mm}$ . In contrast, for the second scribe, we used  $\text{rate}_{\text{feed}} = 30 \text{ mm/s}$ ,  $\text{distance}_{\text{raster}} = 10^{-3} \text{ mm}$ , and  $\text{distance}_{\text{gap}} = 110 \pm 10 \mu\text{m}$ .

### Perovskite deposition

In this work, two different perovskite compositions were used: DMSO/DMF/N<sub>2</sub> and dimethylformamide/*n*-methyl-2-pyrrolidone/diethyl ether (DMF/NMP/DEE). The main body of the work uses the DMSO/DMF/N<sub>2</sub> recipe, whereas the results in [Figure S20](#) uses the DMF/NMP/DEE recipe.

#### DMSO/DMF/N<sub>2</sub>

MAI (158.97 mg) and PbI<sub>2</sub> (461.01 mg) were dissolved in 1 mL of 8:1 ratio DMF:DMSO solvent to obtain a 1 M solution. Prepared substrates were loaded into a glove box, coated with precursor solution, and spun at 1,000 rpm for 5 s, then 5,000 rpm for 20 s; 10 s into the 5,000 rpm cycle, a nitrogen stream was blown onto the substrate from a distance of 1 cm at 100 psi through a tube with a cross-sectional area of 0.32 cm<sup>2</sup>. After the spin cycles were complete, substrates were transferred to a hotplate at 100°C for 45 min.

#### NMP/DMF/DEE

Films were made using a procedure reported previously. Briefly, MAI (127 mg), PbI<sub>2</sub> (368.3 mg), and MAcl (8.09 mg) were dissolved in 9:8 NMP:DMF volume ratio (617.80 μL/549.15 μL) solvent to obtain a 30 wt% solution (excluding MAcl). Substrates were then loaded into the glove box, coated with the precursor solution, and spun at 4,000 rpm for 25 s. Once the spin cycle was stopped, substrates were quickly transferred to a 100 mL bath of DEE. After 1 min in the bath, substrates were removed, quickly blown off with nitrogen, and then placed on top of a petri dish on a 150°C hotplate. After being left to dry on top of the hotplate for 5 min, films were covered with the same petri dish and left to anneal for an addition 3 min. All fabrication and annealing was conducted in a N<sub>2</sub> flowbox.

### Photoemission spectroscopy

During the course of the project, PES results were taken on a number of different instruments, including a Kratos AXIS Nova located at the National Renewable Energy Laboratory (NREL) in Golden, CO, USA; a Physical Electronics 5600 photoelectron spectrometer located at the NREL in Golden, CO, USA; and a Thermo Fisher Scientific Escalab 250xi located at the Institut Lavoisier de Versailles (UMR 8180 CNRS-UVSQ) in Versailles, France. To avoid beam damage, low-power I 3d<sub>5/2</sub>/Pb 4f<sub>7/2</sub> core level measurements were taken with monochromatic 15 W (15 kV, 1 mA) Al K $\alpha$  excitation centered at 1,486.7 eV. In addition to those scans, we conducted typical XPS analysis using the same source at 350 W (15 kV, ~23 mA) and UPS analysis using radiation generated by a He-gas discharge lamp (He I = 21.22 eV). All XPS core level spectra were collected using a step size of 0.1 eV, a high-pass energy (20.00–23.50 eV), and a spot size of ~200 μm, whereas UPS spectra were collected with a step size of 0.05 eV, a pass energy of 1.00–2.95 eV, and a larger spot size. E<sub>F</sub> was calibrated at a sputter-cleaned gold sample. To further rule out possible variation from system to system, we compared consecutive measurements on the same substrate (e.g., I3d<sub>5/2</sub> core level on TiO<sub>x</sub> to NiO<sub>x</sub>). UPS spectra were corrected for

satellite peaks that arise from the polychromatic He I radiation. Core levels were fit using a Gaussian-Lorentzian peak fitting algorithm with a Shirley background. WFs were determined using the intersection between the baseline and a linear fit to the main feature. VBMs were calculated using log extrapolation of the main feature in the valence band region to the background signal. Spectra taken with the Al source are typically assigned an uncertainty of 0.05 eV. Spectra taken with UPS are typically assigned an uncertainty of 0.025 eV. Compositional analyses are typically assigned an uncertainty of 5%. All samples were grounded on both the TiO<sub>x</sub> and NiO<sub>x</sub> contacts during measurements.

### Kelvin probe force microscopy

KPFM measurements were performed using a HORIBA/AIST-NT (TRIOS platform) scanning probe microscopy system. Scans were performed using an Si tip with an Au coating on the detector and tip side (Nanosensors), in amplitude modulation mode (which provides better measurement stability in the presence of significant height variation), in two passes. The first pass scans the sample topography in a non-contact region (~1–5 nm). Then, the probe is lifted by 30 nm to follow the measured topography registering CPD variation over the same area. Each 3 × 3 μm<sup>2</sup> scan was measured from the bottom left corner to the top right; one scan took 30 min to be completed. For laser-based cantilever deflection detection, a 1,310 nm laser diode was used. For the illumination, a 532 nm laser with a nominal power of 10 mW and a spot size of 220 μm were used, providing ~2.7 suns of illumination on the sample. All measurements were completed far from the junction in ambient conditions. All samples were kept in the dark for around 1 h before dark measurements and grounded on both the TiO<sub>x</sub> and NiO<sub>x</sub> contacts during measurements, short-circuiting the device.

### Hyperspectral luminescence imaging

The hyperspectral imaging system records luminescence intensity signal along three dimensions {x, y, λ}. Its main components are the following: a home-built microscope with Thorlabs optomechanical elements, a 2D band-pass filtering system from Photon Etc. with 2 nm resolution, and finally, a 1-Mpix, silicon-based charge-coupled device (CCD) camera PCO1300. The sample is illuminated (λ = 532 nm) through 50× Nikon objective, and the luminescence is collected through the same objective. The excitation beam and luminescence signals are separated with appropriate dichroic beam splitter and filters. The 2D luminescence signal is corrected for each pixel of the sensor from the spectral transmissions along the entire optical path from the read noise and dark current noise of the camera and from the spatial inhomogeneity of the optical system (flat-field). Post-treatment of the data cubes includes a deconvolution and fitting to the generalized Planck law, which is realized with dedicated MATLAB routines. All samples were grounded on both the TiO<sub>x</sub> and NiO<sub>x</sub> contacts during measurements, short-circuiting the device.

### Time-resolved luminescence

Wide-field illumination imaging was realized with a TR-FLIM setup. The system is composed by a pulsed laser Talisker (λ = 532 nm, f = 200 kHz), an intensified electron-multiplied camera CCD (emICCD, PIMAX4, Princeton Instruments), and a home-built opto-mechanical excitation-collection setup. The camera gating time was varied with a 2 ns step from 0 to 1 μs. The photoluminescence was collected through a Nikon 50× objective. The PL is filtered through short-pass and long-pass filters (DMLP650R and FES750, Thorlabs). Acquisitions are post-treated using MATLAB. All samples were grounded on both the TiO<sub>x</sub> and NiO<sub>x</sub> contacts during measurements, short-circuiting the device.

### X-ray absorption spectroscopy

XAS measurements were performed on a Beam Line 8-2 at the Stanford Synchrotron Radiation Lightsource (SSRL) with linearly polarized X-rays at normal and grazing incidence w.r.t. the surface normal. Spectra were collected in total electron yield (TEY) mode via the drain current and normalized by the photon flux on a freshly evaporated gold grid. All samples were grounded on both the  $\text{TiO}_x$  and  $\text{NiO}_x$  contacts during measurements, short-circuiting the device.

### Current density voltage measurements

J-V curves were acquired in air with  $100 \text{ mW/cm}^2$  AM1.5G illumination using a Newport 94083a Solar Simulator and a Keithley 2400 Source Meter. The intensity of the solar simulator was calibrated using an encapsulated Si cell certified by the NREL Cell and Module Characterization group. Because of the unclear active area size, devices were masked to 5 mm (across junction)  $\times$  1 cm (along junction) and illuminated from the perovskite side of the device. Using a four-point probe configuration to eliminate contact resistance, linear-sweep voltammetric scans were taken in the forward direction from  $-0.2 \text{ V}$  to  $1.2 \text{ V}$  and then back at  $0.001 \text{ V/step}$  and  $0.01 \text{ s/step}$ , without prior bias or light soaking in ambient conditions. [Figure S24](#) summarizes that setup.

### SUPPLEMENTAL INFORMATION

Supplemental information can be found online at <https://doi.org/10.1016/j.xcrp.2021.100520>.

### ACKNOWLEDGMENTS

We would like to thank Jeff Christians and Zhen Li for help in fabricating the triple cation ( $\text{FA}_{1-a-b}\text{Cs}_a\text{MA}_b\text{Pb}_{3-x}\text{Br}_x$ ) and  $\text{CsFAPbI}_3$  films in [Figure S21](#). This material is based upon work supported by the U.S. Department of Energy's Office (DOE's) of Energy Efficiency and Renewable Energy (EERE) under the Solar Energy Technologies Office (SETO) project "De-risking halide perovskite solar cells" program (DE-FOA-0000990). The views expressed in the article do not necessarily represent the views of the DOE or the U.S. Government. P.S. acknowledges the French Agence Nationale de la Recherche for funding under contract no. ANR-17-MPGA0012 and the French program of investment for the future (Program d'Investissement d'Avenir, ANRIED-002-01). S.C. would like to thank the European Union's Horizon 2020 research and innovation programme under the Marie Skłodowska-Curie grant agreement N845612 for funding. Use of the Stanford Synchrotron Radiation Lightsource, SLAC National Accelerator Laboratory, is supported by the U.S. Department of Energy, Office of Science, Office of Basic Energy Sciences under Contract No. DE-AC02-76SF00515.

### AUTHOR CONTRIBUTIONS

Conceptualization, J.J.B, K.Z., and P.S.; methodology, S.P.D., A.B., S.C., M.F., G.T., D.N., J.-P.K., J.J.B., and P.S.; software, D.R., J.-B.P., and J.-P.K.; validation, S.P.D. and P.S.; formal analysis, S.P.D., A.B., S.C., M.F., T.K., D.N., and P.S.; investigation, S.P.D., A.B., S.C., M.F., T.K., R.B., F.Z., D.R., D.N., and P.S.; resources, J.-B.P., G.T., J.M.L., M.B., K.Z., M.F.A.M.v.H., J.-P.K., J.J.B., and P.S.; data curation, S.P.D., A.B., S.C., M.F., T.K., and P.S.; writing – original draft, S.P.D., A.B., S.C., and P.S.; writing – review & editing, all authors; visualization, S.P.D., A.B., S.C., T.K., and P.S.; supervision, J.P., M.B., K.Z., M.F.A.M.v.H., J.-P.K., J.J.B. and P.S.; project administration, J.J.B. and P.S.; funding acquisition, J.-B.P., M.B., K.Z., M.F.A.M.v.H., J.-P.K., J.J.B., and P.S.

## DECLARATION OF INTERESTS

The authors declare no competing interests.

## INCLUSION AND DIVERSITY

One or more of the authors of this paper self-identifies as an underrepresented ethnic minority in science.

Received: December 8, 2020

Revised: May 5, 2021

Accepted: July 8, 2021

Published: July 30, 2021

## REFERENCES

- Shao, S., and Loi, M.A. (2020). The role of the interfaces in perovskite solar cells. *Adv. Mater. Interfaces* 7, 1901469.
- Schulz, P., Cahen, D., and Kahn, A. (2019). Halide perovskites: is it all about the interfaces? *Chem. Rev.* 119, 3349–3417.
- Belisle, R.A., Jain, P., Prasanna, R., Leijtens, T., and McGehee, M.D. (2016). Minimal effect of the hole-transport material ionization potential on the open-circuit voltage of perovskite solar cells. *ACS Energy Lett.* 1, 556–560.
- Bertoluzzi, L., Boyd, C.C., Rolston, N., Xu, J., Prasanna, R., O'Regan, B.C., and McGehee, M.D. (2019). Mobile ion concentration measurement and open-access band diagram simulation platform for halide perovskite solar cells. *Joule* 4, 109–127.
- Rau, U., and Kirchartz, T. (2019). Charge carrier collection and contact selectivity in solar cells. *Adv. Mater. Interfaces* 6, 190252.
- Wurfel, U., Cuevas, A., and Würfel, P. (2015). Charge carrier separation in solar cells. *IEEE J. Photovolt* 5, 461–469.
- Brendel, R., and Peibst, R. (2016). Contact selectivity and efficiency in crystalline silicon photovoltaics. *IEEE J. Photovolt* 6, 1413–1420.
- Rakita, Y., Lubomirsky, I., and Cahen, D. (2019). When defects become “dynamic”: Halide perovskites: A new window on materials? *Mater. Horiz.* 6, 1297–1305.
- Yin, W.J., Shi, T., and Yan, Y. (2014). Unusual defect physics in CH<sub>3</sub>NH<sub>3</sub>PbI<sub>3</sub> perovskite solar cell absorber. *Appl. Phys. Lett.* 104, 14864778.
- Kang, J., and Wang, L.W. (2017). High defect tolerance in lead halide perovskite CsPbBr<sub>3</sub>. *J. Phys. Chem. Lett.* 8, 489–493.
- Shi, D., Adinolfi, V., Comin, R., Yuan, M., Alarousu, E., Buin, A., Chen, Y., Hoogland, S., Rothenberger, A., Katsiev, K., et al. (2015). Low trap-state density and long carrier diffusion in organolead trihalide perovskite single crystals. *Science* 347, 519–522.
- Huang, Y., Yin, W.J., and He, Y. (2018). Intrinsic point defects in inorganic cesium lead iodide perovskite CsPbI<sub>3</sub>. *J. Phys. Chem. C* 122, 1345–1350.
- Liu, N., and Yam, C. (2018). First-principles study of intrinsic defects in formamidinium lead triiodide perovskite solar cell absorbers. *Phys. Chem. Chem. Phys.* 20, 6800–6804.
- Steirer, K.X., Schulz, P., Teeter, G., Stevanovic, V., Yang, M., Zhu, K., and Berry, J.J. (2016). Defect tolerance in methylammonium lead triiodide perovskite. *ACS Energy Lett.* 1, 360–366.
- Egger, D.A., Bera, A., Cahen, D., Hodes, G., Kirchartz, T., Kronik, L., Lovrincic, R., Rappe, A.M., Reichman, D.R., and Yaffe, O. (2018). What remains unexplained about the properties of halide perovskites? *Adv. Mater.* 30, e1800691.
- Ceratti, D.R., Rakita, Y., Cremonesi, L., Tenne, R., Kalchenko, V., Elbaum, M., Oron, D., Potenza, M.A.C., Hodes, G., and Cahen, D. (2018). Self-healing inside APbBr<sub>3</sub> halide perovskite crystals. *Adv. Mater.* 30, 1–7.
- Brandt, R.E., Poindexter, J.R., Gorai, P., Kurchin, R.C., Hoye, R.L.Z., Nienhaus, L., Wilson, M.W.B., Polizzotti, J.A., Sereika, R., Žaltauskas, R., et al. (2017). Searching for “defect-tolerant” photovoltaic materials: combined theoretical and experimental screening. *Chem. Mater.* 29, 4667–4674.
- Tirmizi, A.M., Christians, J.A., Dwyer, R.P., Moore, D.T., and Marohn, J.A. (2019). Substrate-dependent photoconductivity dynamics in a high-efficiency hybrid perovskite alloy. *J. Phys. Chem. C* 123, 3402–3415.
- Miller, E.M., Zhao, Y., Mercado, C.C., Saha, S.K., Luther, J.M., Zhu, K., Stevanović, V., Perkins, C.L., and van de Lagemaat, J. (2014). Substrate-controlled band positions in CH<sub>3</sub>NH<sub>3</sub>PbI<sub>3</sub> perovskite films. *Phys. Chem. Chem. Phys.* 16, 22122–22130.
- Olthof, S., and Meerholz, K. (2017). Substrate-dependent electronic structure and film formation of MAPbI<sub>3</sub> perovskites. *Sci. Rep.* 7, 40267.
- Schulz, P., Whittaker-brooks, L.L., Macleod, B.A., Olson, D.C., Loo, Y., and Kahn, A. (2015). Electronic level alignment in inverted organometal perovskite solar cells. *Adv. Mater. Interfaces* 2, 1400532.
- Renna, L.A., Liu, Y., Russell, T.P., Bag, M., and Venkataraman, D. (2018). Evidence of tunable macroscopic polarization in perovskite films using photo-kelvin probe force microscopy. *Mater. Lett.* 217, 308–311.
- Prince, K.J., Nardone, M., Dunfield, S.P., Teeter, G., Mirzokarimov, M., Warren, E.L., Moore, D.T., Berry, J.J., Wolden, C.A., and Wheeler, L.M. (2021). Complementary interface formation toward high-efficiency all-back-contact perovskite solar cells. *Cell Reports Phys. Sci.* 2, 100363.
- Yang, Z., Yan, J., Yang, W., Zeng, Y., Sun, J., Wang, X., Yang, X., Greer, J.C., Sheng, J., Yan, B., et al. (2020). Honeycomb-shaped charge collecting electrodes for dipole-assisted back-contact perovskite solar cells. *Nano Energy* 78, 105362.
- Lin, X., Raga, S.R., Chesman, A.S.R., Ou, Q., Jiang, L., Bao, Q., Lu, J., Cheng, Y.B., and Bach, U. (2020). Honeycomb-shaped charge collecting electrodes for dipole-assisted back-contact perovskite solar cells. *Nano Energy* 67, 104223.
- Song, Y., Bi, W., Wang, A., Liu, X., Kang, Y., and Dong, Q. (2020). Efficient lateral-structure perovskite single crystal solar cells with high operational stability. *Nat. Commun.* 11, 274.
- Zhu, K., Berry, J.J., van Hest, M.F.A.M., Luther, J.M., Schulz, P., and Dameron, A.A. (2019). Heterojunction perovskite photovoltaic devices and methods of making the same. In European patent application publication EP3357101A1, filed October 3, 2015, and published August 8, 2018 and December 12, 2019.
- Ratcliff, E.L., Zacher, B., and Armstrong, N.R. (2011). Selective interlayers and contacts in organic photovoltaic cells. *J. Phys. Chem. Lett.* 2, 1337–1350.
- Ratcliff, E.L., Garcia, A., Paniagua, S.A., Cowan, S.R., Giordano, A.J., Ginley, D.S., Marder, S.R., Berry, J.J., and Olson, D.C. (2013). Investigating the influence of interfacial contact properties on open circuit voltages in organic photovoltaic performance: Work function versus selectivity. *Adv. Energy Mater.* 3, 647–656.
- Boyd, C.C., Shallcross, R.C., Moot, T., Kerner, R., Bertoluzzi, L., Onno, A., Kavadiya, S., Chosy, C., Wolf, E.J., Werner, J., et al. (2020). Overcoming redox reactions at perovskite-nickel oxide interfaces to boost voltages in perovskite solar cells. *Joule* 4, 1759–1775.
- Traore, B., Pedesseau, L., Blancon, J.C., Tretiak, S., Mohite, A.D., Even, J., Katan, C., and Kepenekian, M. (2020). Importance of

- vacancies and doping in the hole-transporting nickel oxide interface with halide perovskites. *ACS Appl. Mater. Interfaces* **12**, 6633–6640.
32. Béchu, S., Ralaiarisoa, M., Etcheberry, A., and Schulz, P. (2020). Photoemission spectroscopy characterization of halide perovskites. *Adv. Energy Mater.* **10**, 1904007.
  33. Zu, F., Amsalem, P., Ralaiarisoa, M., Schultz, T., Schlesinger, R., and Koch, N. (2017). Surface state density determines the energy level alignment at hybrid perovskite/electron acceptors interfaces. *ACS Appl. Mater. Interfaces* **9**, 41546–41552.
  34. Caprioglio, P., Zu, F., Wolff, C.M., Márquez Prieto, J.A., Stolterfoht, M., Becker, P., Koch, N., Unold, T., Rech, B., Albrecht, S., et al. (2019). High open circuit voltages in pin-type perovskite solar cells through strontium addition. *Sustain. Energy Fuels* **3**, 550–563.
  35. Meggiolaro, D., Mosconi, E., and De Angelis, F. (2019). Formation of surface defects dominates ion migration in lead-halide perovskites. *ACS Energy Lett.* **4**, 779–785.
  36. Hu, H., Birkhold, S., Sultan, M., Fakharuddin, A., Koch, S., and Schmidt-Mende, L. (2019). Surface band bending influences the open-circuit voltage of perovskite solar cells. *ACS Appl. Energy Mater.* **2**, 4045–4052.
  37. Conings, B., Baeten, L., De Dobbelaere, C., D'Haen, J., Manca, J., and Boyen, H.G. (2014). Perovskite-based hybrid solar cells exceeding 10% efficiency with high reproducibility using a thin film sandwich approach. *Adv. Mater.* **26**, 2041–2046.
  38. Zu, F.-S., Amsalem, P., Salzmann, I., Wang, R.-B., Ralaiarisoa, M., Kowarik, S., Duhm, S., and Koch, N. (2017). Impact of white light illumination on the electronic and chemical structures of mixed halide and single crystal perovskites. *Adv. Opt. Mater.* **5**, 1700139.
  39. Cui, P., Wei, D., Ji, J., Huang, H., Jia, E., Dou, S., Wang, T., Wang, W., and Li, M. (2019). Planar p–n homojunction perovskite solar cells with efficiency exceeding 21.3%. *Nat. Energy* **4**, 150–159.
  40. de Groot, F., and Kotani, A. (2008). *Core Level Spectroscopy of Solids* (CRC Press).
  41. Stöhr, J. (1992). *NEXAFS Spectroscopy* (Springer).
  42. Stöhr, J., and Outka, D.A. (1987). Determination of molecular orientations on surfaces from the angular dependence of near-edge x-ray-absorption fine-structure spectra. *Phys. Rev. B Condens. Matter* **36**, 7891–7905.
  43. McLeod, J.A., Wu, Z., Shen, P., Sun, B., and Liu, L. (2014). Self-alignment of the methylammonium cations in thin-film organometal perovskites. *J. Phys. Chem. Lett.* **5**, 2863–2867.
  44. Stöhr, J. (1992). *NEXAFS Spectroscopy* (Springer).
  45. Garten, L.M., Moore, D.T., Nanayakkara, S.U., Dwaraknath, S., Schulz, P., Wands, J., Rockett, A., Newell, B., Persson, K.A., Trolrier-McKinstry, S., and Ginley, D.S. (2019). The existence and impact of persistent ferroelectric domains in MAPbI<sub>3</sub>. *Sci. Adv.* **5**, eaas9311.
  46. Widjonarko, N.E., Ratcliff, E.L., Perkins, C.L., Sigdel, A.K., Zakutayev, A., Ndione, P.F., Gillaspie, D.T., Ginley, D.S., Olson, D.C., and Berry, J.J. (2012). Sputtered nickel oxide thin film for efficient hole transport layer in polymer-fullerene bulk-heterojunction organic solar cell. *Thin Solid Films* **520**, 3813–3818.
  47. Ratcliff, E.L., Meyer, J., Steirer, K.X., Garcia, A., Berry, J.J., Ginley, D.S., Olson, D.C., Kahn, A., and Armstrong, N.R. (2011). Evidence for near-surface NiOOH species in solution-processed NiOx selective interlayer materials: impact on energetics and the performance of polymer bulk heterojunction photovoltaics. *Chem. Mater.* **23**, 4988–5000.
  48. Steirer, K.X., Chesin, J.P., Widjonarko, N.E., Berry, J.J., Miedaner, A., Ginley, D.S., and Olson, D.C. (2010). Solution deposited NiO thin-films as hole transport layers in organic photovoltaics. *Org. Electron.* **11**, 1414–1418.
  49. Zhang, F., Silver, S.H., Noel, N.K., Ullrich, F., Rand, B.P., and Kahn, A. (2020). Ultraviolet photoemission spectroscopy and kelvin probe measurements on metal halide perovskites: advantages and pitfalls. *Adv. Energy Mater.* **10**, 1903252.
  50. Teeter, G., Harvey, S.P., Perkins, C.L., Ramanathan, K., and Repins, I.L. (2019). Comparative operando XPS studies of quasi-Fermi level splitting and open-circuit voltage in CZTSe/CdS and CIGS/CdS junctions and device structures. *J. Vac. Sci. Technol. A* **37**, 031202.
  51. Sadewasser, S., and Glatzel, T. (2018). *Kelvin Probe Force Microscopy: From Single Charge Detection to Device Characterization*. (Springer).
  52. Kronik, L., and Shapira, Y. (1999). Surface photovoltage phenomena: theory, experiment, and applications. *Surf. Sci. Rep.* **37**, 1–206.
  53. Leibovitch, M., Kronik, L., Fefer, E., Burstein, L., Korobov, V., and Shapira, Y. (1996). Surface photovoltage spectroscopy of thin films. *J. Appl. Physiol.* **79**, 8549–8556.
  54. Chen, R., Fan, F., Dittrich, T., and Li, C. (2018). Imaging photogenerated charge carriers on surfaces and interfaces of photocatalysts with surface photovoltage microscopy. *Chem. Soc. Rev.* **47**, 8238–8262.
  55. Daboczi, M., Hamilton, I., Xu, S., Luke, J., Limbu, S., Lee, J., McLachlan, M.A., Lee, K., Durrant, J.R., Baikie, I.D., and Kim, J.S. (2019). Origin of open-circuit voltage losses in perovskite solar cells investigated by surface photovoltage measurement. *ACS Appl. Mater. Interfaces* **11**, 46808–46817.
  56. Barnea-Nehoshtan, L., Kirmayer, S., Edri, E., Hodes, G., and Cahen, D. (2014). Surface photovoltage spectroscopy study of organolead perovskite solar cells. *J. Phys. Chem. Lett.* **5**, 2408–2413.
  57. Kronik, L., and Shapira, Y. (2001). Surface photovoltage spectroscopy of semiconductor structures: At the crossroads of physics, chemistry and electrical engineering. *Surf. Interface Anal.* **31**, 954–965.
  58. Schulz, P., Edri, E., Kirmayer, S., Hodes, G., Cahen, D., and Kahn, A. (2014). Interface energetics in organo-metal halide perovskite-based photovoltaic cells. *Energy Environ. Sci.* **7**, 1377–1381.
  59. Tennyson, E.M., Howard, J.M., Roose, B., Garrett, J.L., Munday, J.N., Abate, A., and Leite, M.S. (2019). The effects of incident photon energy on the time-dependent voltage response of lead halide perovskites. *Chem. Mater.* **21**, 8969–8976.
  60. Aristidou, N., Eames, C., Sanchez-Molina, I., Bu, X., Kosco, J., Islam, M.S., and Haque, S.A. (2017). Fast oxygen diffusion and iodide defects mediate oxygen-induced degradation of perovskite solar cells. *Nat. Commun.* **8**, 15218.
  61. Cacovich, S., Messou, D., Bercegol, A., Béchu, S., Yaiche, A., Shafique, H., Rousset, J., Schulz, P., Bouttemy, M., and Lombez, L. (2020). Light-induced passivation in triple cation mixed halide perovskites: interplay between transport properties and surface chemistry. *ACS Appl. Mater. Interfaces* **12**, 34784–34794.
  62. Delamarre, A., Lombez, L., and Guillemoles, J.F. (2012). Contactless mapping of saturation currents of solar cells by photoluminescence. *Appl. Phys. Lett.* **100**, 8–11.
  63. Bercegol, A., El-Hajje, G., Ory, D., and Lombez, L. (2017). Determination of transport properties in optoelectronic devices by time-resolved fluorescence imaging. *J. Appl. Physiol.* **122**, 15005164.
  64. Katahara, J.K., and Hillhouse, H.W. (2014). Quasi-Fermi level splitting and sub-bandgap absorptivity from semiconductor photoluminescence. *J. Appl. Physiol.* **116**, 1489346.
  65. Paul, N., Le-Guen, V., Ory, D., and Lombez, L. (2017). Numerical model to extract materials properties map from spectrally resolved luminescence images. In *Proceedings of the 2017 IEEE 44th Photovoltaic Specialist Conference* (Curran Associates), pp. 70–74.
  66. Stolterfoht, M., Wolff, C.M., Márquez, J.A., Zhang, S., Hages, C.J., Rothhardt, D., Albrecht, S., Burn, P.L., Meredith, P., Unold, T., et al. (2018). Visualization and suppression of interfacial recombination for high-efficiency large-area pin perovskite solar cells. *Nat. Energy* **3**, 847–854.